Influence of Cation Species on Thermal Expansion of $Y_2Si_2O_7$-$Gd_2Si_2O_7$ Solid Solutions

Jamesa L. Stokes[a,†], Cameron J. Bodenschatz[a], Bryan J. Harder[a], Valerie L. Wiesner[b], Wissam A. Saidi[c,d], and Douglas E. Wolfe[e,f,g,h,i]

[a] NASA Glenn Research Center, Cleveland, OH 44135, USA

[b] NASA Langley Research Center, Hampton, VA 23666, USA

[c] Mechanical Engineering and Materials Science Department, The University of Pittsburgh, Pittsburgh, PA, 15261, USA

[d] National Energy Technology Laboratory, Pittsburgh, PA, 15236, USA

[e] Applied Research Laboratory, The Pennsylvania State University, University Park, PA, 16802, USA

[f] Materials Science and Engineering Department, The Pennsylvania State University, University Park, PA, 16802, USA

[g] Ken and Mary Alice Lindquist Nuclear Engineering Department, The Pennsylvania State University, University Park, PA, 16802, USA

[h] Engineering Science and Mechanics Department, The Pennsylvania State University, University Park, PA, 16802, USA

[i] Additive Manufacturing and Design Department, The Pennsylvania State University, University Park, PA, 16802, USA

[†] Corresponding author. Email address: jamesa.l.stokes@nasa.gov Telephone: 1-216-433-5874

Abstract

Mixtures of $Y_2Si_2O_7$ and $Gd_2Si_2O_7$ were synthesized by solid-state reaction at 1600°C and characterized via *in situ* x-ray diffraction (XRD) to determine their coefficients of thermal expansion (CTE). All solid solutions within the system exhibited the orthorhombic δ-$RE_2Si_2O_7$

($Pna2_1$) structure. Thermal expansion measurements of $Y_2Si_2O_7$ and $Gd_2Si_2O_7$ correlated well with reported values in literature, and all synthesized solid solutions exhibited CTEs between $Y_2Si_2O_7$ and $Gd_2Si_2O_7$. Generally, there was a slight decrease in CTE exhibited by the materials with increasing $Gd_2Si_2O_7$ content, with $Gd_2Si_2O_7$ having the lowest CTEs and $Y_2Si_2O_7$ the highest CTEs. The decrease in CTE was attributed to stronger bonds of Gd-O over Y-O, as determined by calculated crystal orbital Hamilton populations using density functional theory. However, such differences were very small and crystal structure was the dominating factor in CTE trends.

Keywords: Rare earth silicates, $Y_2Si_2O_7$, $Gd_2Si_2O_7$, thermal expansion, density functional theory, electronic structure

1 Introduction

The crystal structures of rare earth (RE) disilicates are primarily dependent on their cation size and annealing temperature [1]. Due to their unique electron configuration, their size often influences their chemistry in various systems and resulting properties. Tuning properties by creating solid solutions of these materials is a recent development in incorporating them in different applications. There has been a preference for studies of mixtures of smaller RE disilicates [2,3] due to the high-temperature stability of the Type C structure (β-$RE_2Si_2O_7$) [4]. However, the applicability of larger RE disilicates in applications such as multifunctional coating systems [5,6] and phosphor materials [7,8] prompted interest in investigation of the properties of blended smaller and larger disilicate structures. The authors previously carried out *in situ* x-ray diffraction (XRD) experiments on solid solutions in the $Yb_2Si_2O_7$-$Gd_2Si_2O_7$ system [9] to determine the influences of varying cations on lattice expansion as a function of temperature in the polymorphs. While thermal expansion behavior was largely governed by crystal structure (as also shown to be the case for monolithic $RE_2Si_2O_7$ materials [10–12]), minor variations attributed to changes in

lattice volume drove the desire for additional inquiry into possible mechanisms of expansion that is caused by the presence of varying cations in the same crystal structure. Moreover, recent studies into the role of electronic structure on unit cell volume and potential consequences to expansion in RE monosilicates [13] have prompted further questions of the influence of cation species (particularly electronic configuration) on disilicate mixture properties.

The current work seeks to support ongoing investigations in understanding the properties of solid solutions of disilicates by examining the yttrium disilicate-gadolinium disilicate ($Y_2Si_2O_7$-$Gd_2Si_2O_7$) system using a combination of experimental and computational methods. Unlike the $Yb_2Si_2O_7$-$Gd_2Si_2O_7$ system, which do not share a common structure, $Y_2Si_2O_7$ and $Gd_2Si_2O_7$ can share two polymorphs on the Felsche diagram (low temperature Type B α-$RE_2Si_2O_7$ ($P\bar{1}$) and high temperature Type E δ-$RE_2Si_2O_7$ ($Pna2_1$)), suggesting for the formation of a complete solid solution in this system. However, it is also important to note that while yttrium itself is often grouped with the rare earth elements due to similar size and properties, a key distinguishing feature of the lanthanides is their filling of the 4f orbital, resulting in poor shielding of the strong nuclear charge to outer electrons [14]. Given that orbital bandwidth may be correlated with a lowered expansion anisotropy in some RE silicate systems [13], this prompted further interest to closely examine the differences in electronic structure between Y^{3+} and Gd^{3+} and how that may affect structural and thermal properties in $Yb_2Si_2O_7$-$Gd_2Si_2O_7$ system or monolithic disilicate materials. Thus, by utilizing density functional theory (DFT) for structure optimization, electronic density of states, and chemical bonding calculations, it is anticipated that electronic structure contributions to thermal expansion within the $Y_2Si_2O_7$-$Gd_2Si_2O_7$ system will also be elucidated.

2 Experimental Procedures and Methods

2.1 Materials Synthesis

Yttrium disilicate ($Y_2Si_2O_7$, YDS) spray dried powder was obtained from Praxair, Inc. (99%). Analysis of the as-received YDS powder indicated that the powder was not single-phase, consisting of crystalline β-YDS and yttrium monosilicate (Y_2SiO_5). This powder was heat treated at 1600°C for 10 hours (5°C/min heating and cooling rate), resulting in single phase Type D γ-YDS ($P2_1/c$) and indicating that there was possibly some amorphous SiO_2 in the starting powder that had not fully reacted with possible Y_2O_3 precursors during the spray dry process. Orthorhombic Type E δ-YDS was synthesized by heat treating the as-received YDS powder at 1700°C for 5 hours (20°C/min heating and cooling rate). Gadolinium oxide (Gd_2O_3) (HEFA Rare Earth Canada Inc., 99.99%) and silicon oxide (SiO_2, Alfa Aesar, 99.5%) were used to synthesize single phase gadolinium disilicate (δ-$Gd_2Si_2O_7$, GdDS) by a solid-state reaction method. The oxides were weighed out in their respective ratios and mixed on a ball mill in ethanol for 24 hours using 10 mm cylindrical zirconium oxide (ZrO_2) milling media. The mixed powders were then dried and pressed into 25.4 mm pellets. These pellets were heat treated at 1600°C for 10 hours to react the oxides and obtain δ-GdDS. $Y_{2-2x}Gd_{2x}Si_2O_7$ ($0 \leq x \leq 0.30$) solutions were synthesized via a solid-state reaction route using the previously described disilicate powders. γ-YDS was mixed with δ-GdDS on a ball mill in ethanol using 2 mm spherical ZrO_2 milling media. The mixtures were dried on a hot plate and uniaxially pressed into ~1 g, 12.7 mm diameter pellets. To react the disilicate powders, the pellets were heat treated at 1600°C for 10 hours. A pellet of each composition was crushed into powder for diffraction analysis, while additional pellets were mounted in epoxy and polished for microscopic analyses.

2.2 Characterization

Scanning electron microscopy (SEM) and energy dispersive spectroscopy (EDS) (Thermo Fisher FEI Q250 Environmental SEM, Phenom ProX) were utilized to obtain images of the microstructure and compositions of reaction products, respectively. Crystallographic phases were determined on post-heat-treated samples by *ex situ* XRD on an Empyrean diffractometer (Malvern PANalytical) using cobalt radiation (Co Kα = 1.789 Å) and analyzed in Jade 10 software with the International Center for Diffraction Data (ICDD) crystallographic database. Coefficients of thermal expansion (CTEs) and high temperature stability of the resulting solid solutions were determined using *in situ* diffraction in the Empyrean diffractometer using a hot stage (Anton Paar HTK 2000N). National Institutes of Standards Technology (NIST) standard reference material (SRM) cerium oxide (CeO_2) powder was used as a calibration standard to determine the platinum heating strip temperature set points, as outlined in our previous publication [9]. Once temperature set points were determined, the sample powders were mixed with isopropanol and dispersed onto the heating strip. Scans were taken over a 2θ range of 10° to 100° at temperatures of 25°C, 200°C, 400°C, 600°C, 800°C, 1000°C, 1200°C, 1300°C, 1400°C, and 1500°C. All scans were then analyzed in TOPAS [15] using the LeBail method [16] to estimate the lattice parameters of the materials at each temperature. The average bulk CTE is approximated as 1/3 of the unit cell volume expansion coefficient (i.e., ΔV vs. ΔT divided by 3).

2.3 Density Functional Theory (DFT)

Structure optimizations and electronic density of states calculations were performed using plane-wave DFT as implemented in the Vienna Ab-initio Simulation Package (VASP) [17–20]. Core electrons were modeled using the Projector Augmented-Wave (PAW) pseudopotentials [21–23], while valence electrons were modeled using the Perdew-Burke-Ernzerhof exchange-

correlation functional modified for solids (PBEsol) [24,25]. Gd was modeled with 18 valence electrons in the configuration $[1s^2 2s^2 2p^6 3s^2 3p^6 3d^{10} 4s^2 4p^6 4d^{10}] 5s^2 5p^6 6s^2 4f^7 5d^1$, Y was modeled with 11 valence electrons in the configuration $[1s^2 2s^2 2p^6 3s^2 3p^6 3d^{10}] 4s^2 4p^6 5s^2 4d^1$, Si was modeled with 4 valence electrons in the configuration $[1s^2 2s^2 2p^6] 3s^2 3p^2$, and O was modeled with 6 valence electrons in the configuration $[1s^2] 2s^2 2p^4$. The wavefunctions were represented with planewaves using a cutoff energy of 520 eV to expand the wavefunctions of the system. Brillouin zone integrations were performed using automatically generated Γ-centered *k*-point meshes of 5×4×2 for geometry optimizations and 10×6×4 for electronic density of states calculations, equating to 1500 *k*-points per reciprocal atom (KPPRA) and 10,000 KPPRA, respectively. [26]. The tetrahedron method with Blöchl corrections was used for partial occupancy smearing. Calculations were spin-polarized, and the electronic structure convergence tolerance was 1×10^{-8} eV. Structure optimizations were performed until the residual forces between atoms decreased below 1×10^{-4} eV/Å. The electronic density of states and Crystal Orbital Hamilton Populations [27–29] of the optimal structures were then calculated. Initial δ-phase conventional standard structures were obtained from the Materials Project database [30]. Individual site substitutions were performed for dopant positions within the crystal structure at 12.5 and 25 mol% to find the lowest energy structure at each concentration.

3 Results and Discussion

3.1 $Y_{2-2x}Gd_{2x}Si_2O_7$ at 1600°C

XRD scans of the $Y_{2-2x}Gd_{2x}Si_2O_7$ series are plotted in Figure 1(a). Starting at 5 mol%, additions of GdDS to γ-YDS immediately resulted in a phase transformation from γ-$RE_2Si_2O_7$ to δ-$RE_2Si_2O_7$. XRD analysis indicated a single-phase structure, suggesting complete solubility of GdDS into δ-YDS. All solid solutions in this study exhibited the δ-$RE_2Si_2O_7$ structure. *Maier et*

al. investigated mixtures of YDS with various disilicates [31] and showed that incorporation of 25 mol% of GdDS to YDS at 1600°C also resulted in the δ-YDS structure, agreeing with results in this study. As GdDS content increased across this series, the peaks in the XRD data shifted towards smaller angles while maintaining this single-phase structure (as shown in the inset in Figure 1(a)), which suggested an expansion of the lattice. The measured lattice parameters of the δ materials are listed in Table 1 and the measured changes in lattice parameters are plotted in Figure 1(b), showing overall increase with increase in GdDS content. While the *a* and *b* lattice directions exhibited similar increases in length, the c direction of the unit cell exhibited the highest magnitude of extension as a function of GdDS content.

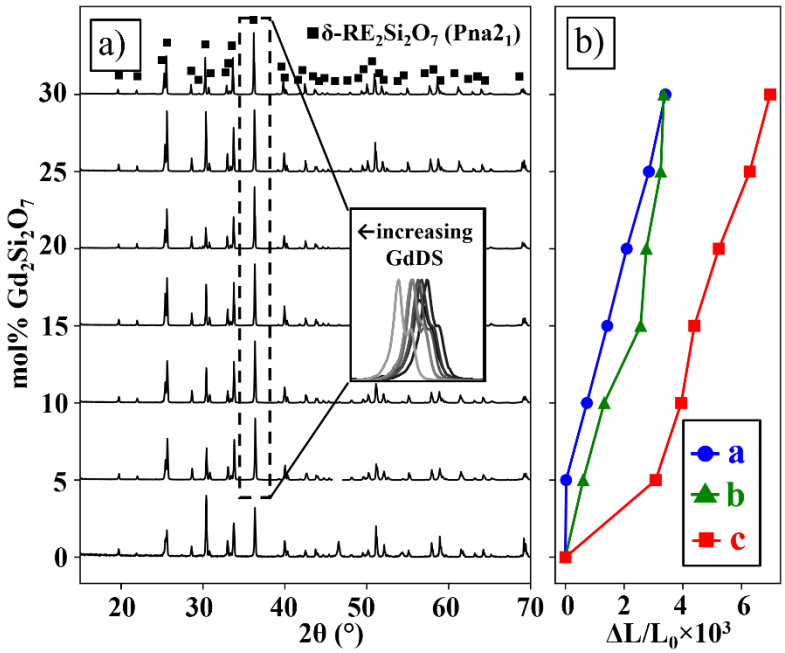

Figure 1. a) XRD scans of $Y_{2-2x}Gd_{2x}Si_2O_7$ after heat treatment at 1600°C, 10 hours with an inset graph showing shift in peaks with increasing GdDS content. b) Graph of the change of the a (circle), b (triangle), and c (square) lattice parameters of the δ-$RE_2Si_2O_7$ materials from 0 mol% to 30 mol% GdDS. L_0 values for the lattice parameters are taken from XRD analysis of synthesized δ-$Y_2Si_2O_7$ in this study (analyzed with powder diffraction file (PDF) card #04-002-6023 of δ-$Y_2Si_2O_7$).[32]

Table 1. Measured lattice parameters and calculated unit cell volumes of $RE_2Si_2O_7$ materials in this study.

	mol% GdDS	a (Å)	b (Å)	c (Å)	Volume (Å^3)
$Y_2Si_2O_7$	0	13.667±0.006	5.020±0.003	8.152±0.001	559.295

$Y_{1.9}Gd_{0.1}Si_2O_7$	5	13.680±0.002	5.016±0.003	8.165±0.007	560.273
$Y_{1.8}Gd_{0.2}Si_2O_7$	10	13.690±0.003	5.019±0.002	8.172±0.007	561.499
$Y_{1.7}Gd_{0.3}Si_2O_7$	15	13.700±0.006	5.026±0.001	8.176±0.005	562.968
$Y_{1.6}Gd_{0.4}Si_2O_7$	20	13.709±0.008	5.027±0.002	8.183±0.001	563.933
$Y_{1.5}Gd_{0.5}Si_2O_7$	25	13.719±0.001	5.029±0.007	8.191±0.003	565.120
$Y_{1.4}Gd_{0.6}Si_2O_7$	30	13.727±0.004	5.030±0.009	8.197±0.002	565.976
$Gd_2Si_2O_7$ [9]	100	13.863±0.003	5.054±0.007	8.300±0.002	581.528

Back-scattered electron (BSE) micrographs of the pellet cross sections are displayed in Figure 2. BSE micrographs of the grain structure showed slight changes in morphology as GdDS content increased. At 5 and 10 mol% GdDS (Figure 2(a) and Figure 2(b)), the grain size distribution seemed to be bimodal, with larger grains surrounded by very fine grains. Overall, the grains exhibited an elongated morphology. At 15 mol% GdDS (Figure 2(c)), a ~5X increase in grain size was observed from the 5 mol% sample. These much larger grains were observed at 20, 25 and 30 mol% GdDS (Figures 2(d), (e), and (f)). EDS results indicated that while the crystal structure was single-phase, no phase segregation of Y- or Gd-rich δ-$RE_2Si_2O_7$ phases were observed, correlating well with XRD observations of a complete solid solution series. The images of the microstructure also showed a considerable amount of transgranular cracking. This cracking could have been the result of the γ-YDS to δ-YDS phase transformation and the volumetric expansion of the unit cell that occurs in this transformation (~2%) [10,32].

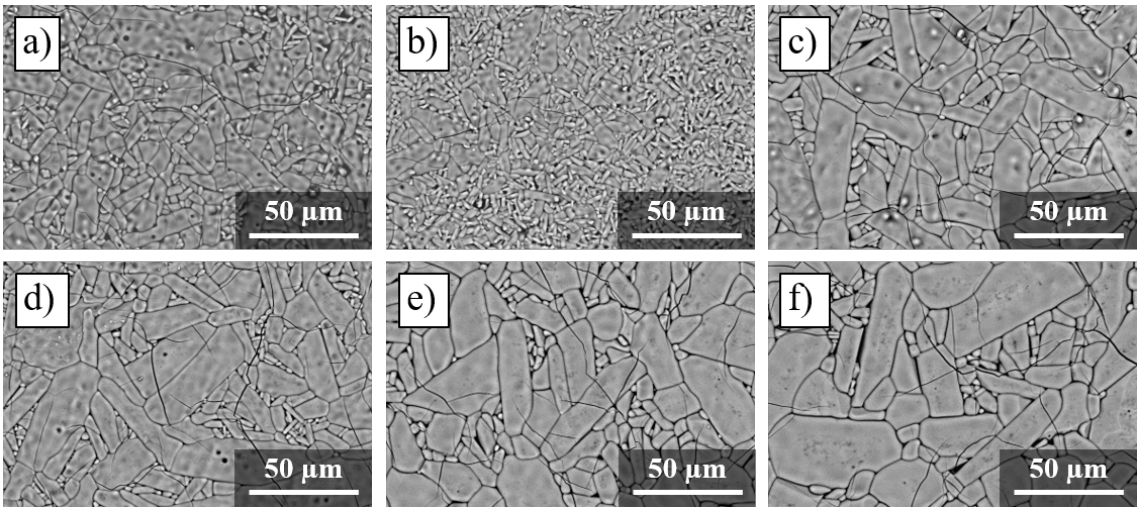

Figure 2. BSE micrographs of grain structure of synthesized a) $Y_{1.9}Gd_{0.1}Si_2O_7$, b) $Y_{1.8}Gd_{0.2}Si_2O_7$, c) $Y_{1.7}Gd_{0.3}Si_2O_7$, d) $Y_{1.6}Gd_{0.4}Si_2O_7$, e) $Y_{1.5}Gd_{0.5}Si_2O_7$, and f) $Y_{1.4}Gd_{0.6}Si_2O_7$.

The δ-$RE_2Si_2O_7$ structure is intrinsic to YDS at higher temperatures above ~1650°C [33,34]. The γ-$RE_2Si_2O_7$ polymorph of YDS is more stable over a wider range of temperatures (~1300°C-1650°C), and heat treatment of this material at 1600°C did not result in any phase transformation (Figure 1(a)). However, the addition of GdDS to YDS seemed to stabilize the δ-$RE_2Si_2O_7$ polymorph at a slightly lower temperature than predicted on the *Felsche* diagram [4]. This observation could be expected, given that δ-$RE_2Si_2O_7$ is the only stable polymorph of GdDS above ~1400°C. Because YDS can also exist in this structure, solid solutions in this series should all possess this polymorph with further changes in structure related to lengthening of lattice parameters correlating with additions of GdDS to the unit cell. The molar volumes of the YDS-GdDS solid solutions were determined and plotted in Figure 3. A drop in molar volume was observed with phase transformations as GdDS was added in solution. The addition of GdDS to γ-YDS at only 5 mol% resulted in the immediate γ→δ phase transformation. The accompanying molar volume decrease from this transformation is similar to the analogous temperature-dependent phase transformation from undoped γ-YDS to δ-YDS, as displayed in Figure 3. Overall, this behavior suggested optimization of the structures by allowing for unit cell expansion and

pyrosilicate anion $[Si_2O_7]^{6-}$ distortion while keeping the volume occupied by each formula unit of the solid solution to a minimum. [4]

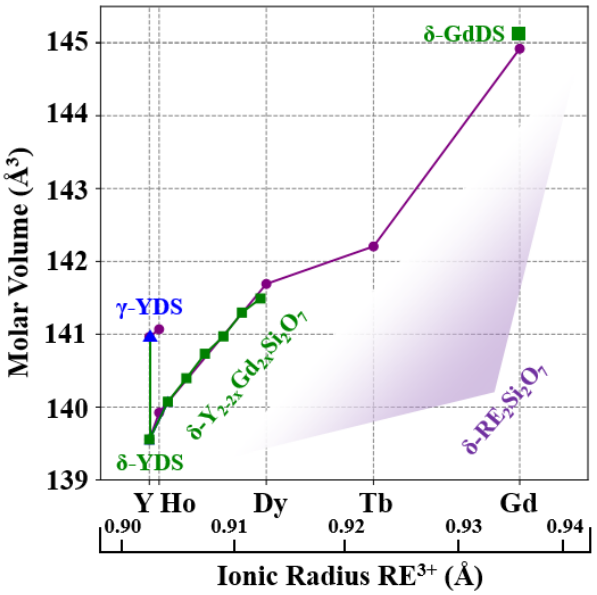

Figure 3. Molar volume graph of $Y_{2-2x}Gd_{2x}Si_2O_7$ solid solutions synthesized in this study (blue (triangle) and green (square) markers and lines) and monolithic $RE_2Si_2O_7$ structures (purple (circle) markers and lines) from literature.[10,32,35–39]

It is important to note that all materials were synthesized at 1600°C in this study, and a full $Y_2Si_2O_7$-$Gd_2Si_2O_7$ binary diagram was not determined. However, current results along with trends from literature can provide insights of what can be expected at different temperatures. As previously discussed, YDS can have four different polymorphs as a function of temperature, although, according to the Felsche diagram, it is expected that polymorphism would be reduced with substitution of larger cations. Addition of 5 mol% GdDS resulted in an average cation size of 0.902 Å, slightly larger than Ho^{3+} and within a region of the Felsche diagram in which the β-$RE_2Si_2O_7$ structure is no longer stable at any temperature. At this cation size, there are still three polymorphs present as a function of temperature: γ-$RE_2Si_2O_7$, δ-$RE_2Si_2O_7$, and α-$RE_2Si_2O_7$. In the case of γ-$RE_2Si_2O_7$, a very narrow region of stability exists around ~1350-1400°C, with α-$RE_2Si_2O_7$ expected to form below this range and δ-$RE_2Si_2O_7$ above this range. Larger cations

would be expected to form α-$RE_2Si_2O_7$ at same temperature, suggesting than additions of 5 mol% or less of GdDS would be needed if the γ-$RE_2Si_2O_7$ structure was desired from YDS-GdDS solid solutions.

The δ-$RE_2Si_2O_7$ structure has been briefly discussed, and as stated, is expected to be the crystal structure of a compete solid solution series for the YDS-GdDS system at temperatures above ~1400°C. At lower temperatures, larger RE disilicates between Y^{3+} and Gd^{3+} are expected to form α-$RE_2Si_2O_7$, a unique pyrosilicate structure that does not contain double tetrahedra Si_2O_7 units but instead isolated SiO_4 tetrahedra and Si_3O_{10} silicate chains. This difference in silicate structure may indicate that a reconstructive phase transformation must take place, as studies have noted its limited stability due to sluggish kinetics of crystallization. [40,41] For GdDS, this structure is expected to be stable below ~1500°C. For undoped YDS, this structure is expected at ~1200°C and lower. However, in *in situ* XRD analysis of both materials (discussed in the following section), the phase was not observed to form, and in the case of YDS, δ-YDS destabilized readily to β-YDS at lower temperatures, correlating with other observations in literature on the slow formation [40–42]. α-$RE_2Si_2O_7$ is a shared polymorph between YDS and GdDS, and it is hypothesized that these two disilicates can also form a complete solid solution series with this structure below ~1400°C (similar to the δ-$RE_2Si_2O_7$ structure demonstrated in this study), although it is unclear how doping would affect formation kinetics. Because the goal of these investigations was to understand properties of single-phase YDS-GdDS materials and the stability of α-$RE_2Si_2O_7$ is predicated on kinetics of formation, the synthesis of this structure was outside of scope of this paper.

3.2 Temperature Stability and Thermal Expansion

No indication of phase destabilization was observed for GdDS or the solid solutions synthesized in this study. However, extraneous peaks were observed in the *in situ* XRD analysis of δ-YDS. The *in situ* XRD scans from room temperature to 1500°C are displayed in Figure 4. Extra peaks were observed to form during analysis at 1300°C around 32° 2θ. These peaks continued to grow in magnitude with increasing temperature, indicating additional formation up to 1500°C and were still present upon cooling to room temperature. The additional peaks observed in the *in situ* XRD scans were indicative of the formation of the Type C β-$RE_2Si_2O_7$ polymorph (C2/m) of YDS at 1300°C, which is consistent with thermodynamic prediction of the phase stability of this structure (δ-YDS is formed above ~1650°C, whereas β-YDS is stable from ~1200-1350°C) [34]. Unlike the δ-$Y_{2-2x}Gd_{2x}Si_2O_7$ solid solutions, however, undoped δ-YDS began to transform to β-YDS once heated to 1300°C, suggesting that the addition of GdDS to δ-YDS aided in stabilizing this high temperature polymorph below its synthesis temperature.

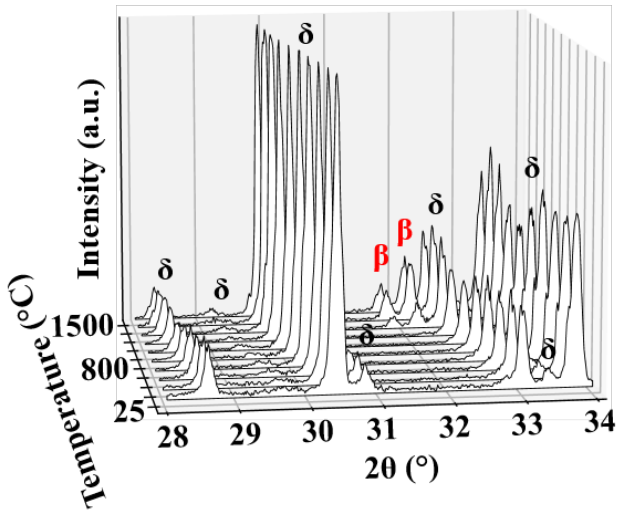

Figure 4. *In situ* XRD graphs of δ-$Y_2Si_2O_7$ up to 1500°C. Peaks corresponding to the formation of β-$Y_2Si_2O_7$ appear at 1300°C, highlighted by the red symbols.

The bulk CTEs of all the disilicates investigated in this study are listed in Table 2 and organized in ascending order by "average" cation size. An "average" cation size of the solid

solutions was estimated by adding together sizes of the cations weighted by their relative amounts in each composition (i.e., $\chi_a r_a+\chi_b r_b=r_{avg}$ where χ is mol%). The thermal expansion graphs are plotted in Figure 5, and third-order polynomial coefficients of fitted CTE curves for each lattice direction of each sample can be found in the supplemental data (Table S1). The *a* and *b* lattice directions of γ-YDS exhibited very similar expansion as a function of temperature, with the *c* direction expanding the least up to 1500°C (Figure 5(a)). In undoped δ-YDS (Figure 5(b)), the *a* and *b* directions expanded ~2X more than γ-YDS. The average bulk CTE of undoped δ-YDS was 8.11×10^{-6}/K, correlating well with values reported in literature (~8.1×10^{-6}/K up to 1400°C [10]).

Out of all the orthorhombic δ-$RE_2Si_2O_7$ materials in this study, undoped δ-YDS exhibited the highest bulk CTE and undoped δ-GdDS (Figure 5(g)) exhibited the lowest. It is important to note that the *c* expansion in particular of GdDS itself was an order of magnitude lower (0.31×10^{-6}/K) than both undoped δ-YDS (2.41×10^{-6}/K) and the YDS-GdDS solid solutions. Interestingly, the addition of GdDS also decreased the magnitude of the *a* and *b* expansion of the mixtures, although the expansion was still less that YDS. The addition of GdDS to YDS did not result in any discernable trends in CTEs as a function of dopant content, although the bulk CTE values of all the solid solutions fell between YDS and GdDS. To further understand the expansion behavior of RE disilicates in this crystal structure, orthorhombic dysprosium disilicate (δ-$Dy_2Si_2O_7$, DyDS) was also synthesized, and *in situ* XRD was used to determine its CTEs. The average bulk CTE of δ-DyDS was determined to be 7.54×10^{-6}/K (Table 2), which agrees well with literature values [11]. The average cation size estimated for $Y_{1.4}Gd_{0.6}Si_2O_7$ (0.911Å) is approximately equal to that of Dy^{3+} (0.912Å) (and roughly equal molar volume), and this solid solution exhibited slightly greater average bulk expansion than δ-DyDS.

Table 2. Volumetric and average bulk thermal expansion coefficients ($\times10^{-6}$/K) of $RE_2Si_2O_7$ materials synthesized in this study up to 1500°C.

	mol% GdDS	Structure	Average RE cation size (Å)	Volumetric Expansion Coefficient	Average Bulk Coefficient
$Y_2Si_2O_7$	0	Monoclinic (γ)	0.900	13.77±0.41	4.59±0.14
$Y_2Si_2O_7$	0	Orthorhombic (δ)	0.900	24.32±0.73	8.11±0.21
$Y_{1.8}Gd_{0.2}Si_2O_7$	10	Orthorhombic (δ)	0.904	23.68±0.47	7.89±0.24
$Y_{1.7}Gd_{0.3}Si_2O_7$	15	Orthorhombic (δ)	0.906	23.23±0.69	7.74±0.23
$Y_{1.5}Gd_{0.5}Si_2O_7$	25	Orthorhombic (δ)	0.909	23.88±0.60	7.96±0.24
$Y_{1.4}Gd_{0.6}Si_2O_7$	30	Orthorhombic (δ)	0.911	23.47±0.70	7.82±0.31
$Dy_2Si_2O_7$	----	Orthorhombic (δ)	0.912	22.63±0.67	7.54±0.19
$Gd_2Si_2O_7$[9]	100	Orthorhombic (δ)	0.938	21.77±0.54	7.25±0.22

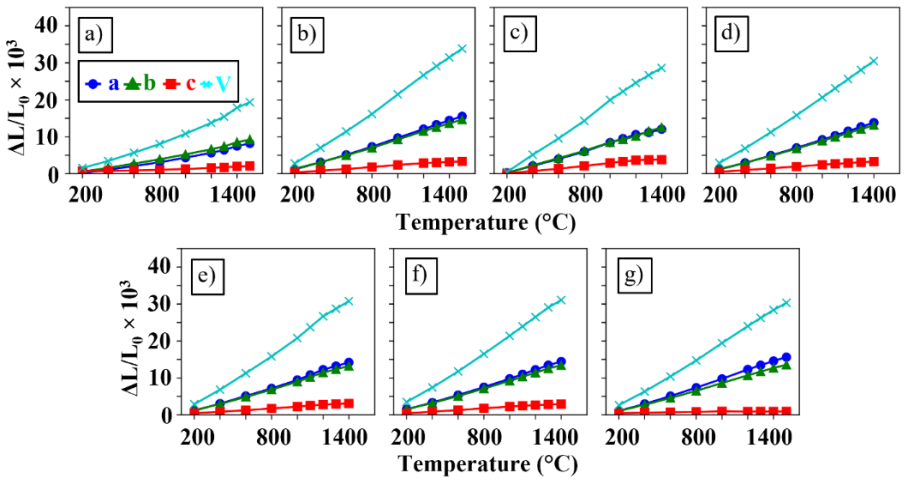

Figure 5. Graphs of thermal expansion as a function of temperature for a) γ-$Y_2Si_2O_7$, b) δ-$Y_2Si_2O_7$, c) δ-$Y_{1.8}Gd_{0.2}Si_2O_7$ (10 mol% GdDS), d) δ-$Y_{1.7}Gd_{0.3}Si_2O_7$ (15 mol% GdDS), e) δ-$Y_{1.5}Gd_{0.5}Si_2O_7$ (25 mol% GdDS), f) δ-$Y_{1.4}Gd_{0.6}Si_2O_7$ (30 mol% GdDS), and g) δ-$Gd_2Si_2O_7$.

3.3 Considerations of Cation Species on Bond Strength and Properties

Between the three undoped materials, there was a reverse trend in CTE than what was expected, with δ-YDS exhibiting the largest CTE and GdDS the smallest. It was previously hypothesized that the changes in volume in the disilicate solid solutions due to cation substitution possibly resulted in changes in thermal expansion [9], given that phonon frequencies are volume dependent within the quasi-harmonic approximation of lattice vibrations [43]. In the monolithic δ-$RE_2Si_2O_7$ materials, the average bulk CTE was observed to decrease with increasing molar volume (i.e. YDS>DyDS>GdDS), and these results suggested that with increasing molar volume of the

composition, the tendency of the lattice to further expand as a function of temperature might be reduced. In the case of δ-YDS, because each formula unit occupies a smaller volume within the unit cell, the amount of distortion allowed within each cell as a function of temperature is possibly higher compared to GdDS, which possesses a higher molar volume. However, size and mass of cations can play a role in phonon scattering. As listed in Table 2, the Gd^{3+} cation is ~4% larger than Y^{3+}, and ~55% heavier in atomic mass (157.25 g/mol for Gd vs. 88.91 g/mol for Y). The greater effect that Gd can have in scattering phonons could result in Gd-O being less affected by vibration modes that can induce lattice expansion.

In the monolithic δ-$RE_2Si_2O_7$ materials, DyDS>GdDS could be related to the RE-O bond dissociation energy, with Gd being slightly greater than Dy [44]. A greater bond strength indicates that the RE-O bonds need more energy to activate phonon modes, resulting in less distortion as a function of temperature. The RE-O bond dissociation energy for Gd-O is in fact slightly higher than Y-O (714 kJ/mol for Y vs. 715 kJ/mol for Gd) [44]. Another factor to consider is the stability of YDS in the δ-$RE_2Si_2O_7$ structure. As previously mentioned, the δ-$RE_2Si_2O_7$ structure is a high-temperature polymorph of YDS (Figure 6). Due to the vibrational modes of cations at high temperature, structures with high-coordination and high-symmetry are better stabilized for smaller cations like Y^{3+} [45]. The thermochemical stability of $RE_2Si_2O_7$ materials has not been extensively studied in literature, although the enthalpy of formation of γ-YDS has been reported to be -67 kJ/mol (formation from Y_2O_3 and SiO_2)[34]. Such an assessment could be beneficial in determining the structural stability of YDS and other $RE_2Si_2O_7$ materials in varying crystal structures [46–50]. Within the orthorhombic structure, if the bonds are already stretched within the lattice to stabilize the crystal structure, then they may be weaker and susceptible to further perturbation with temperature, hence potentially greater thermal expansion of δ-YDS compared to

δ-GdDS. Thus, structural stability could also be a factor in resulting material properties. If δ-GdDS is thermochemically more stable than δ-YDS, that could mean that the bonds in GdDS are less susceptible to perturbation with temperature, resulting in lower thermal expansion.

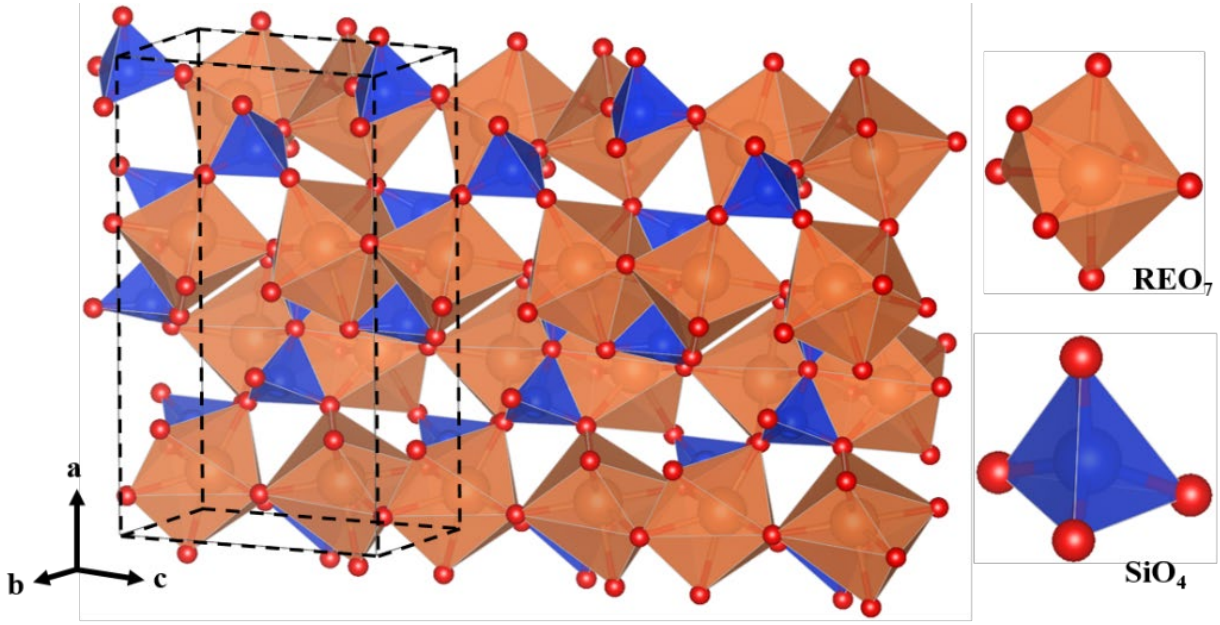

Figure 6. δ-$RE_2Si_2O_7$ $Pna2_1$ structure[32], plotted in VESTA[51]. The unit cell is highlighted by the black dashed lines. This crystal structure is arranged as RE-O_7 polyhedra in two sets of double chains (edge-shared within the chains, corner shared between the chains). The double chain units are connected through Si_2O_7 double tetrahedra and expand along the *c* axis. The higher density of RE-O bonds along the *c* direction could explain why the *c* direction was more sensitive to changes in expansion as GdDS was added.

DFT calculations were carried out on δ-$RE_2Si_2O_7$ solid solutions to understand possible electronic structure contributions to the current thermal expansion results. Table 3 lists the lattice parameters and unit cell volume of the optimized structures of select δ-$RE_2Si_2O_7$ solid solutions compared to experimental lattice parameters from XRD. DFT calculations also were performed on a 12.5 mol% composition, although it was not synthesized. As there were eight RE atoms in the simulation cell, it was only possible to do substitutions in 12.5 mol% increments. Thus, 12.5 mol% was the minimum GdDS content allowed for calculations and was similar to 10 and 15 mol% synthesized samples. As listed in Table 3, the lattice parameters and volume increased as a function of GdDS content, as expected. The calculated *a* and *c* lattice parameters were slightly

smaller than what was observed in the experimentally determined structures, while the calculated *b* lattice parameters were slightly higher than experimental values.

Table 3. Comparison of lattice parameter values between DFT calculations and values extracted from XRD scans of δ-$RE_2Si_2O_7$ materials synthesized in this study.

mol% GdDS	Composition	Lattice Parameters (Å) and Volume (Å^3)	Experiment	DFT	ΔExp-DFT
0	δ-$Y_2Si_2O_7$	a	13.667	13.618	0.049
		b	5.020	5.027	-0.007
		c	8.152	8.121	0.031
		V	559.295	555.945	3.350
12.5	δ-$Y_{1.75}Gd_{0.25}Si_2O_7$	a	----	13.642	----
		b	----	5.0315	----
		c	----	8.138	----
		V	----	558.590	----
25	δ-$Y_{1.5}Gd_{0.5}Si_2O_7$	a	13.719	13.666	0.053
		b	5.029	5.036	-0.006
		c	8.191	8.154	0.037
		V	565.120	561.174	3.946
100	δ-$Gd_2Si_2O_7$	a	13.863 [9]	13.807	0.056
		b	5.054 [9]	5.062	-0.009
		c	8.300 [9]	8.256	0.044
		V	581.528	577.020	4.507

Generally, PBEsol characteristically underestimates lattice parameters, but exhibits better energetic representation of solids over other methods. [24,25] Also, DFT calculations were carried out at 0 K, so smaller lattice parameters of the calculated structures were somewhat expected. DFT at 0 K is commonly used in the literature to calculate thermodynamic properties, mechanical properties, and bond strengths at finite temperatures. While it is true that the electronic structure is likely to change with increased temperature, this change is more heavily influenced by the changes in the crystal structure than electron excitation, and therefore the

changes should be small for similar crystal structures. The bond strength predicted at 0 K will influence the phonon vibrations, which will subsequently influence the change in crystal structure and CTE. Beyond the thermal expansion, there were no observed changes in crystal phase at increased temperature. Any crystal structure-based changes should result in only small shifts in the electronic structure. Thus, the bond strength predicted by 0 K DFT should correlate to the CTE even at high temperatures.

Originally, density of states (DOS) calculations from DFT were investigated, as DOS can be used as an indicator of chemical bond strength, as strength is related to the band gap, i.e., the amount of energy required to move an electron from the valence band to the conduction band [52–54]. A shift to more negative valence band energy with respect to the Fermi level also indicates a more energetically favorable electronic structure. An increase in magnitude of the number of states at a given energy can indicate increased orbital overlap in that region which also corresponds to stronger chemical bonding. Figure 7 displays the total d-orbital DOS plots Figure 7(a), as well as individual DOS contributions of the Y^{3+} and Gd^{3+} d-orbitals (Figure 7(b) and Figure 7(c), respectively).

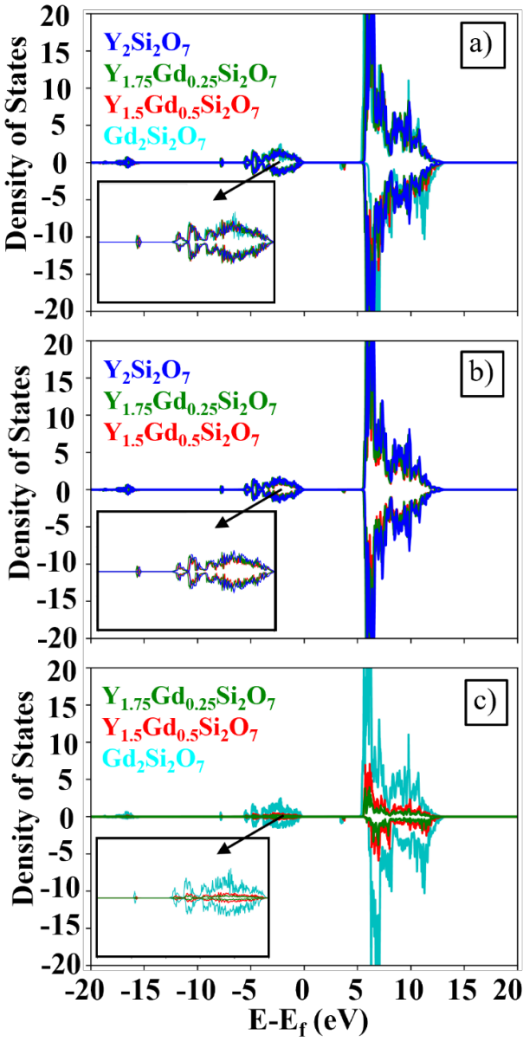

Figure 7. d-orbital plots of a) total density of states b) Y^{3+} density of states and c) Gd^{3+} density of states.

From the total d-orbital DOS, additions of Gd did not result in significant shifts in orbital energies. With decreasing GdDS content, there was a decrease in magnitude of Gd d-orbital DOS. This was somewhat expected, as the decrease in Gd atoms in the lattice would decrease overall contributions of Gd to electron density. Similarly, the Y^{3+} d-orbital DOS plot (Figure 7(b)) exhibited a decrease in magnitude with decreasing YDS content. Although the increase in Gd content does appear to shift the band energies to the left, the shift is quite small, and it is difficult to elucidate from these plots whether any shift would have a meaningful impact. The decrease in the magnitude of states in Figure 7(c) is expected due to the decrease in the number of Gd atoms present, although the

trend does not appear to be proportional to the number of Gd atoms which could indicate an impact on bond strength as well.

To assess the relative bond strengths within the crystal structures identified here, the crystal orbital Hamilton populations (COHPs) were calculated to quantify the occupation of bonding and anti-bonding states for select YDS-GdDS mixtures. Per-bond values allowed for comparison across different compositions and numbers of bonds. The projected COHPs (plotted in Figure 8) integrated up to the Fermi level (IpCOHPs) on a per-bond basis for YDS, 12.5 mol% GdDS, 25 mol% GdDS, and GdDS are listed in Table 4. In this analysis, more negative IpCOHP values correlate to stronger bonds. The IpCOHPs were calculated for two scenarios: the first includes all electrons (AE) included within the PAW potentials (previously listed in the experimental procedures), and the second includes standard valence electron (VE) orbitals ($5s^2 4d^1$ for Y; $6s^2 5d^1$ for Gd; $3s^2 3p^2$ for Si; $2s^2 2p^4$ for O). We will refer to these two cases as AE and VE, respectively. In the two approximations to IpCOHPs, the Si—O bond had the largest value, suggesting that Si—O bonds were the strongest, which corresponds well with existing literature [11,55–62]. Y—O had a slightly stronger bond than Gd—O when considering AE in computing IpCOHPs, which is consistent with greater electron shielding from the additional 4f orbitals in the Gd electronic structure. However, across the concentration range, Y—O and Gd—O bonds are fairly similar in terms of IpCOHP (and therefore bond strength), with a maximum difference of ~0.03 eV/bond for the AE cases and even smaller (~0.01 eV/bond) for VE. These differences are similar to values that are considered negligible in other literature reports [63,64]. We also note that Si—O bonds had much more negative IpCOHP values, indicating stronger bonds than both Y—O and Gd—O bonds.

Table 4. Integrated projected crystal orbital Hamilton populations (IpCOHPs) on a per-bond basis of select mixtures. The integration for the valence electron columns was from -7 – 0 eV with respect to the Fermi level.

mol% GdDS	IpCOHP/bond (all DFT electrons)					IpCOHP/bond (valence electrons)				
	All	Si—O	Y—O	Gd—O	YGd-O	All	Si—O	Y—O	Gd—O	YGd-O
0	−4.666	−7.950	−2.789	--	-2.789	−1.569	−1.912	−1.373	--	-1.373
12.5	−4.661	−7.955	−2.785	−2.731	-2.778	−1.572	−1.909	−1.371	−1.443	-1.380
25	−4.656	−7.960	−2.782	−2.724	-2.768	−1.576	−1.907	−1.370	−1.438	-1.387
100	−4.629	−7.991	--	−2.707	-2.707	−1.597	−1.892	--	−1.429	-1.429

We also examined IpCOHP values for cation—O bonds across the Gd doping concentration range for cation subsets, including: 1) all cation—oxygen bonds (Si—O, Y—O, and Gd—O); 2) Si—O bonds; 3) Y—O bonds; 4) Gd—O bonds; and 5) Y—O and Gd—O bonds. In most cases, the magnitude of the IpCOHP decreases with increasing Gd content, implying weaker bonding. This is contrary to the trend in CTE, as weaker bonding would typically indicate a larger CTE, which is opposite of the trend we observed. However, the IpCOHP values for standard VE increased in magnitude (i.e., become more negative) for the cases including all of the cations and the case including Y—O and Gd—O bonds for increasing GdDS content. This correlates with the observed trend in CTE. We note that the differences in calculated IpCOHP here are still small as mentioned above, but the observed trends indicate that the bond strength as determined by the IpCOHP could be an explanation for the trend in CTE as a function of Gd mol%. These results also indicated the need to be careful when considering electron orbitals in the calculation of bond strength. Also, further analysis may also be warranted to understand the magnitude of bond strength variation in disilicate-disilicate calculations and subsequent effects on the small differences also observed in the experimental expansion data. While these changes may be considered minuscule in other materials systems as listed previously, it is currently unclear if they are of appreciable impact in this solid solution system.

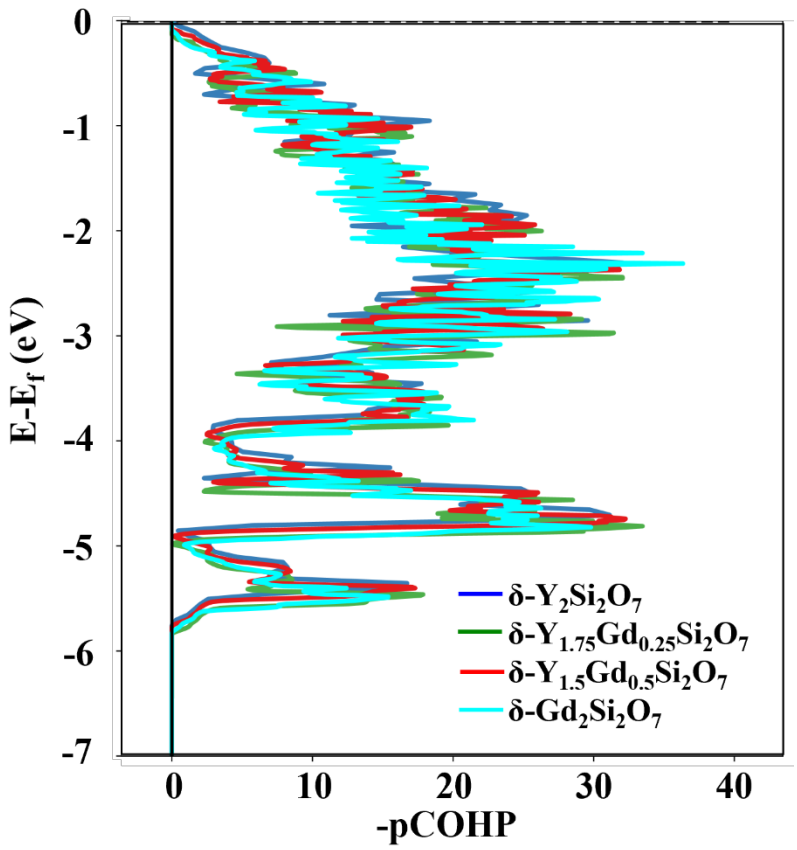

Figure 8. Projected crystal orbital Hamilton populations (IpCOHPs) for all Y—O and Gd—O bonds as a function of energy and Gd doping concentration for standard valence electrons integrated from -7 to 0 eV.

The thermal expansion results do not deviate greatly from previous studies of thermal expansion of disilicates as well as the authors' own previous investigation of the YbDS-GdDS system [9,11]. In our previous investigation of YbDS-GdDS solid solutions, bulk thermal expansion behavior was largely governed by crystal structure. In the current study, the addition of GdDS demonstrated that there were small changes in anisotropic expansion observed based on cation substitution, but arrangement of cation-oxygen bonds in the structure ultimately determined bulk expansion response in disilicate systems. This does not, however, imply that other materials properties cannot be greatly affected by cation species. In particular, thermal conductivity of many systems, including disilicates [5,65], can be influenced by mixing cations in solid solution. Thus, mixtures of disilicates could be optimized to keep changes in thermal expansion to a minimum

while influencing other materials properties such as thermal conductivity by changing the size and mass of the constituents. DFT results on the lattice constants correlated well with experimental results for the investigated systems. Further, while the DOS and IpCOHPs investigations provided good insight into the electronic structure of systems, these were not generally conclusive in rationalizing the thermal expansion difference between YDS and GdDS, although other DFT methods to calculate enthalpy of formation of these materials may be key in determining how structural stability affects material properties. Future studies into electronic structure influence can also include cation charge distribution and orbital filling and could be instrumental in determining differences in bond strength within solid solutions.

4 Conclusions

The thermal expansion behavior and high temperature equilibria of the $Y_{2-2x}Gd_{2x}Si_2O_7$ up to 30 mol% $Gd_2Si_2O_7$ were assessed to support ongoing efforts in understanding the properties of various disilicate solid solutions for many applications. The orthorhombic δ-$RE_2Si_2O_7$ structure was exhibited by all solid solutions synthesized in this study heat treated at 1600°C. Crystal structure largely governed CTE response of the materials up to 1500°C, although with the addition of GdDS, solid solutions exhibited slightly smaller CTEs than monolithic YDS, as well as lower anisotropy between lattice directions. Crystal orbital Hamilton population calculations using DFT indicated that Gd-O bonds may be slightly stronger than Y-O bonds in this crystal structure, leading to a lower CTE of GdDS when compared to YDS. As the first comprehensive study done on high temperature solid solutions in this system, this study can contribute to continuing efforts to understand the properties and behavior of RE disilicates and disilicate-disilicate mixtures.

Acknowledgements

This work was supported under the NASA Transformational Tools and Technologies (TTT) Project as a part of the Transformative Aeronautics Concepts Program (TACP).

References

[1] J. Felsche, The crystal chemistry of the rare-earth silicates, in: Rare Earths. Struct. Bond., Springer, 1973: pp. 99–197. https://doi.org/10.1007/3-540-06125-8_3.

[2] A. Escudero, M.D. Alba, A.I. Becerro, Polymorphism in the Sc2Si2O7-Y2Si2O7system, J. Solid State Chem. 180 (2007) 1436–1445. https://doi.org/10.1016/j.jssc.2006.11.029.

[3] A.J. Fernández-Carrión, M.D. Alba, A. Escudero, A.I. Becerro, Solid solubility of Yb2Si2O7 in β-, γ- and δ-Y2Si2O7, J. Solid State Chem. 184 (2011) 1882–1889. https://doi.org/10.1016/j.jssc.2011.05.034.

[4] J. Felsche, Polymorphism and crystal data of the rare-earth disilicates of type R.E.2Si2O7, J. Less-Common Met. 21 (1970) 1–14. https://doi.org/10.1016/0022-5088(70)90159-1.

[5] L.R. Turcer, N.P. Padture, Towards multifunctional thermal environmental barrier coatings (TEBCs) based on rare-earth pyrosilicate solid-solution ceramics, Scr. Mater. 154 (2018) 111–117. https://doi.org/10.1016/j.scriptamat.2018.05.032.

[6] J.L. Stokes, B.J. Harder, V.L. Wiesner, D.E. Wolfe, Effects of crystal structure and cation size on molten silicate reactivity with environmental barrier coating materials, J. Am. Ceram. Soc. 103 (2020) 622–634. https://doi.org/10.1111/jace.16694.

[7] H. Feng, D. Ding, H. Li, S. Lu, S. Pan, X. Chen, G. Ren, Cerium concentration and temperature dependence of the luminescence of Lu2Si2O7:Ce scintillator, J. Alloys Compd. 509 (2011) 3855–3858. https://doi.org/10.1016/j.jallcom.2010.12.124.

[8] V.P. Hedaoo Raikwar, V.B. Bhatkar, S.K. Omanwar, Combustion synthesis and photoluminescence in novel red emitting yttrium gadolinium pyrosilicate nanocrystalline

phosphor, J. Alloys Compd. 672 (2016) 653–659. https://doi.org/10.1016/j.jallcom.2016.02.203.

[9] J.L. Stokes, B.J. Harder, V.L. Wiesner, D.E. Wolfe, Crystal structures and thermal expansion of Yb2Si2O7–Gd2Si2O7 solid solutions, J. Solid State Chem. 312 (2022) 123166. https://doi.org/10.1016/j.jssc.2022.123166.

[10] M.D. Dolan, B. Harlan, J.S. White, M. Hall, S.T. Misture, S.C. Bancheri, B. Bewlay, Structures and anisotropic thermal expansion of the α, β, γ, and δ polymorphs of Y2Si2O7, Powder Diffr. 23 (2008) 20–25. https://doi.org/10.1154/1.2825308.

[11] A.J. Fernández-Carrión, M. Allix, A.I. Becerro, Thermal expansion of rare-earth pyrosilicates, J. Am. Ceram. Soc. 96 (2013) 2298–2305. https://doi.org/10.1111/jace.12388.

[12] K. Fukuda, H. Matsubara, Thermal expansion of delta Y2Si2O7, J. Am. Ceram. Soc. 87 (2004) 89–92.

[13] M. V Ayyasamy, P. V Balachandran, Correlation between d -orbital bandwidth and local coordination environment in RE 2 SiO 5 compounds with implications in minimizing the coefficient of thermal expansion anisotropy (RE = Sc, Y, La), AIP Adv. 12 (2022) 045012. https://doi.org/10.1063/5.0085482.

[14] V.M. Goldschmidt, T.F.W. Barth, Geochemische Verteilungsgesetze der Elemente. 5. Isomorphie und Polymorphie des Sesquioxyde, Ja. Dybwad, Oslo, Kristiania, 1925.

[15] A.A. Coelho, TOPAS and TOPAS-Academic: An optimization program integrating computer algebra and crystallographic objects written in C++: An, J. Appl. Crystallogr. 51 (2018) 210–218. https://doi.org/10.1107/S1600576718000183.

[16] A. Le Bail, H. Duroy, J.L. Fourquet, Ab-initio structure determination of LiSbWO6 by X-

ray powder diffraction, Mater. Res. Bull. 23 (1988) 447–452. https://doi.org/10.1016/0025-5408(88)90019-0.

[17] G. Kresse, J. Furthmüller, Efficiency of ab-initio total energy calculations for metals and semiconductors using a plane-wave basis set, Comput. Mater. Sci. 6 (1996) 15–50. https://doi.org/10.1016/0927-0256(96)00008-0.

[18] G. Kresse, J. Furthmüller, Efficient iterative schemes for ab initio total-energy calculations using a plane-wave basis set, Phys. Rev. B. 54 (1996) 11169–11186. https://doi.org/10.1103/PhysRevB.54.11169.

[19] G. Kresse, J. Hafner, Ab initio molecular dynamics for liquid metals, Phys. Rev. B. 47 (1993) 558–561. https://doi.org/10.1103/PhysRevB.47.558.

[20] G. Kresse, J. Hafner, Ab initio molecular-dynamics simulation of the liquid-metal-amorphous-semiconductor transition in germanium, Phys. Rev. B. 49 (1994) 14251–14269. https://doi.org/10.1103/PhysRevB.49.14251.

[21] G. Kresse, J. Hafner, Norm-conserving and ultrasoft pseudopotentials for first-row and transition elements, J. Phys. Condens. Matter. 6 (1994) 8245–8257. https://doi.org/10.1088/0953-8984/6/40/015.

[22] P.E. Blöchl, Projector Augmented-Wave Method, Phys. Rev. B. 50 (1994) 17953–17979. https://doi.org/10.1103/PhysRevB.50.17953.

[23] G. Kresse, D. Joubert, From ultrasoft pseudopotentials to the projector augmented-wave method, Phys. Rev. B. 59 (1999) 1758–1775. https://doi.org/10.1103/PhysRevB.59.1758.

[24] J.P. Perdew, A. Ruzsinszky, G.I. Csonka, O.A. Vydrov, G.E. Scuseria, L.A. Constantin, X. Zhou, K. Burke, Restoring the density-gradient expansion for exchange in solids and surfaces, Phys. Rev. Lett. 100 (2008). https://doi.org/10.1103/PhysRevLett.100.136406.

[25] J.P. Perdew, A. Ruzsinszky, G.I. Csonka, O.A. Vydrov, G.E. Scuseria, L.A. Constantin, X. Zhou, K. Burke, Erratum: Restoring the density-gradient expansion for exchange in solids and surfaces (Physical Review Letters (2008) 100 (136406)), Phys. Rev. Lett. 102 (2009) 39902. https://doi.org/10.1103/PhysRevLett.102.039902.

[26] H.J. Monkhorst, J.D. Pack, Special points for Brillouin-zone integrations, Phys. Rev. B. 13 (1976) 5188–5192.

[27] R. Dronskowski, P.E. Blochl, Crystal Orbital Hamilton Populations (COHP). Energy-Resolved Visualization of Chemical Bonding in Solids Based on Density-Functional Calculations, J. Phys. Chem. 97 (1993) 8617–8624.

[28] V.L. Deringer, A.L. Tchougréeff, R. Dronskowski, Crystal orbital Hamilton population (COHP) analysis as projected from plane-wave basis sets, J. Phys. Chem. A. 115 (2011) 5461–5466. https://doi.org/10.1021/jp202489s.

[29] S. Maintz, V.L. Deringer, A.L. Tchougréeff, R. Dronskowski, LOBSTER: A tool to extract chemical bonding from plane-wave based DFT, J. Comput. Chem. 37 (2016) 1030–1035. https://doi.org/10.1002/jcc.24300.

[30] A. Jain, S.P. Ong, G. Hautier, W. Chen, W.D. Richards, S. Dacek, S. Cholia, D. Gunter, D. Skinner, G. Ceder, K.A. Persson, Commentary: The materials project: A materials genome approach to accelerating materials innovation, APL Mater. 1 (2013). https://doi.org/10.1063/1.4812323.

[31] N. Maier, G. Rixecker, K.G. Nickel, Formation and stability of Gd , Y , Yb and Lu disilicates and their solid solutions, J. Solid State Chem. 179 (2006) 1630–1635. https://doi.org/10.1016/j.jssc.2006.02.019.

[32] G. V Anan'eva, V.E. Karapetyan, A.M. Korovkin, T.I. Merkulyaeva, I.A. Peschanskaya,

I.R. Savinova, P.P. Feofilov, Structural Characteristics and Physics Properties of Crystals of Diortho (Pyro) Silicates of Lanthanides, Yttrium and Scnadium Grown byt the Czochralski Method, Inorg. Mater. 18 (1982) 442–445.

[33] J. Felsche, Crystal data on the polymorphic disilicate Y2Si2O7, Naturwissenschaften. 57 (1970) 127–128. https://doi.org/10.1007/BF00600051.

[34] H. Mao, M. Selleby, O. Fabrichnaya, Thermodynamic reassessment of the Y2O3-Al2O3-SiO2 system and its subsystems, Calphad Comput. Coupling Phase Diagrams Thermochem. 32 (2008) 399–412. https://doi.org/10.1016/j.calphad.2008.03.003.

[35] G. V Anan'eva, A.M. Korovkin, T.I. Merkulyaevaa, A.M. Morozova, M. V Petrov, I.R. Savinova, V.R. Startsev, P.P. Feofilov, Growth of Lanthanide Oxyorthosilicate Single Crytals, and their Structural and Optical Characteristics, Inorg. Mater. 17 (1981).

[36] Y.I. Smolin, Y.F. Shepelev, The crystal structures of the rare earth pyrosilicates, Acta Crystallogr. Sect. B. 26 (1970) 484–492. https://doi.org/10.1107/S0567740870002698.

[37] J. Smolin, Y. Shepelev, Structure determination of erbium pyrosilicate, Izvs. Akad. Nauk. SSSR. Neorg. Mater. 4 (1968).

[38] A.N. Christensen, Investigation by the use of profile refinement of nuetron powder diffraction data of the geometry of the [Si2O7]6- ions in the high-temperature phases of rare-earth disilicates prepared from the melt in crucible-free synthesis, Zeitschrift Fur Krist. 209 (1994) 7–13.

[39] A. Maqsood, B.M. Wanklyn, G. Garton, Flux growth of polymorphic rare-earth disilicates, R2Si2O7 (R = Tm, Er, Ho, Dy), J. Cryst. Growth. 46 (1979) 671–680. https://doi.org/10.1016/0022-0248(79)90185-4.

[40] A. Escudero, A.I. Becerro, Stability of the low temperature polymorphs (y and a) of Lu-

doped Y2Si2O7, J. Phys. Chem. Solids. 68 (2007) 1348–1353. https://doi.org/10.1016/j.jpcs.2007.02.028.

[41] M.E. Fleet, X. Liu, Rare earth disilicates R2Si2O7 (R = Gd, Tb, Dy, Ho): type B, Zeitschrift Für Krist. - Cryst. Mater. 218 (2003) 795–801. https://doi.org/10.1524/zkri.218.12.795.20550.

[42] G. Bocquillon, C. Chateau, C. Loriers, J. Loriers, Polymorphism under pressure of the disilicates of the heavier lanthanoids Ln2Si2O7 (Ln = Tm, Yb, Lu), J. Solid State Chem. 20 (1977) 135–141. https://doi.org/10.1016/0022-4596(77)90060-3.

[43] M.T. Dove, Introduction to Lattice Dynamics, Cambridge University Press, New York, 1994. http://aapt.scitation.org/doi/10.1119/1.17708.

[44] Y. Luo, Comprehensive Handbook of Chemical Bond Energies, CRC Press, Boca Raton, 2007.

[45] S. Trolier-McKinstry, R.E. Newnham, Materials Engineering, Cambridge University Press, 2017. https://doi.org/10.1017/9781316217818.

[46] G. Costa, B.J. Harder, N.P. Bansal, B.A. Kowalski, J.L. Stokes, Thermochemistry of calcium rare-earth silicate oxyapatites, J. Am. Ceram. Soc. 103 (2020) 1446–1453. https://doi.org/10.1111/jace.16816.

[47] G.C.C. Costa, N.S. Jacobson, Thermochemistry of Rare Earth Silicates for Environmental Barrier Coatings, in: Int. Conf. Expo Adv. Ceram. Compos., Daytona Beach, FL, 2015. http://ntrs.nasa.gov/archive/nasa/casi.ntrs.nasa.gov/20150004112.pdf%5Cnhttp://ntrs.nasa.gov/archive/nasa/casi.ntrs.nasa.gov/20150007887.pdf%5Cnhttps://drive.google.com/open?id=0B0fTxDBXtHZMZFlnRTlhUl9LdzQ.

[48] G. Costa, B.J. Harder, N.P. Bansal, J.L. Stokes, K. Lilova, T. Subramani, S. V. Ushakov,

K.J. Meisner, A. Navrotsky, Energetics of reactions between ceramic coating materials and their binary oxide components with silicate melts, J. Am. Ceram. Soc. (2022) 1–11. https://doi.org/10.1111/jace.18715.

[49] S. Yang, M. Powell, J.W. Kolis, A. Navrotsky, Thermochemistry of rare earth oxyhydroxides, REOOH (RE = Eu to Lu), J. Solid State Chem. 287 (2020) 121344. https://doi.org/10.1016/j.jssc.2020.121344.

[50] S.M. Hosseini, A. Navrotsky, Energetic effects of substitution of La-Nd and Si-Ge oxyapatite-type materials, J. Am. Ceram. Soc. 96 (2013) 3915–3919. https://doi.org/10.1111/jace.12705.

[51] K. Momma, F. Izumi, VESTA 3 for three-dimensional visualization of crystal, volumetric and morphology data, J. Appl. Crystallogr. 44 (2011) 1272–1276. https://doi.org/10.1107/S0021889811038970.

[52] G. V. Gibbs, F.C. Hill, M.B. Boisen, R.T. Downs, Power law relationships between bond length, bond strength and electron density distributions, Phys. Chem. Miner. 25 (1998) 585–590. https://doi.org/10.1007/s002690050151.

[53] R.F. Zhang, S. Veprek, A.S. Argon, Anisotropic ideal strengths and chemical bonding of wurtzite BN in comparison to zincblende BN, Phys. Rev. B - Condens. Matter Mater. Phys. 77 (2008) 4–7. https://doi.org/10.1103/PhysRevB.77.172103.

[54] A.H. Reshak, G. Lakshminarayana, J. Ebothe, A.O. Fedorchuk, M.F. Fedyna, H. Kamarudin, P. Mandracci, S. Auluck, Band structure, density of states, and crystal chemistry of ZrGa 2 and ZrGa3 single crystals, J. Alloys Compd. 556 (2013) 259–265. https://doi.org/10.1016/j.jallcom.2012.12.138.

[55] M. Cameron, S. Sueno, C.T. Prewitt, J.J. Papike, High-Temperature crystal chemistry of

acmite, diopside, hedenbergite, jadeite, spodumene, and Ureyite, Am. Mineral. 58 (1973) 594–618.

[56] J.R. Smith, An Orthopyroxene Structure Up to 850°C, Am. Mineral. 58 (1973) 636–648.

[57] G.E. Brown, C.T. Prewitt, S. Brook, N. York, High-Temperature Crystal Chemistry of Hortonolite, 58 (1973) 577–587.

[58] D.R. Peacor, High-Temperature, Single-Crystal X-ray Study of Natrolite, Am. Mineral. 58 (1973) 676–680.

[59] J.R. Smith, High Temperature Crystal Chemistry of Fayalite, Am. Mineral. 60 (1975) 1092–1097.

[60] S. Sueno, M. Cameron, C.T. Prewitt, Orthoferrosilite; high-temperature crystal chemistry, Am. Mineral. 61 (1976) 38–53.

[61] E.P. Meagher, The Crystal Structures of Pyrope and Grossularite at Elevated Temperatures, Am. Mineral. 60 (1975) 218–228.

[62] R.M. Hazen, Effects of temperature and pressure on the crystal structure of ferromagnesian olivine, Am. Mineral. 62 (1977) 286–295.

[63] V. Singh, D.T. Major, Electronic Structure and Bonding in Co-Based Single and Mixed Valence Oxides: A Quantum Chemical Perspective, Inorg. Chem. 55 (2016) 3307–3315. https://doi.org/10.1021/acs.inorgchem.5b02426.

[64] B.B. Dumre, S. V. Khare, Interrelationship of bonding strength with structural stability of ternary oxide phases of MgSnO3: A first-principles study, Phys. B Condens. Matter. 637 (2022) 413896. https://doi.org/10.1016/j.physb.2022.413896.

[65] L.R. Turcer, A. Sengupta, N.P. Padture, Low thermal conductivity in high-entropy rare-earth pyrosilicate solid-solutions for thermal environmental barrier coatings, Scr. Mater.

191 (2021) 40–45. https://doi.org/10.1016/j.scriptamat.2020.09.008.